Front. Earth Sci. 2019, 13(4): 836–847
https://doi.org/10.1007/s11707-019-0784-6

RESEARCH ARTICLE

A new technique for automatically locating the center of tropical cyclones with multi-band cloud imagery

Xiaoqin LU (✉)[1], Hui YU[1], Xiaoming YANG[2], Xiaofeng LI[3,4], Jie TANG[1]

1 Shanghai Typhoon Institute, China Meteorological Administration, Shanghai 200030, China
2 Ocean Department, Shanghai Ocean University, Shanghai 201306, China
3 CAS Key Laboratory of Ocean Circulation and Waves, Institute of Oceanology, Chinese Academy of Sciences, Qingdao 266071, China
4 Center for Ocean Mega-Science, Chinese Academy of Sciences, Qingdao 266071, China

© Higher Education Press and Springer-Verlag GmbH Germany, part of Springer Nature 2019

Abstract A spiral cloud belt matching (SCBeM) technique is proposed for automatically locating the tropical cyclone (TC) center position on the basis of multi-band geo-satellite images. The technique comprises four steps: fusion of multi-band geo-satellite images, extraction of TC cloud systems, construction of a spiral cloud belt template (CBT), and template matching to locate the TC center. In testing of the proposed SCBeM technique on 97 TCs over the western North Pacific during 2012–2015, the median error (ME) was 50 km. An independent test of another 29 TCs in 2016 resulted in a ME of 54 km. The SCBeM performs better for TCs with intensity above "typhoon" level than it does for weaker systems, and is not suitable for use on high-latitude or landfall TCs if their cloud band formations have been destroyed by westerlies or by terrain. The proposed SCBeM technique provides an additional solution for automatically and objectively locating the TC center and has the potential to be applied conveniently in an operational setting. Intercomparisons between the Automated Rotational Center Hurricane Eye Retrieval (ARCHER) and SCBeM methods using events from 2014 to 2016 reveal that ARCHER has better location accuracy. However, when IR imagery alone is used, the ME of SCBeM is 54 km, and in the case of low latitudes and low vertical wind shear the ME is 45–47 km, which approaches that of ARCHER (49 km). Thus, the SCBeM method is simple, has good time resolution, performs well and is a better choice for those TC operational agencies in the case that the microwave images, ASCAT, or other observations are unavailable.

Keywords tropical cyclone, center location, geostationary satellite, matching technique

Received April 4, 2019; accepted July 29, 2019

E-mail: luxq@typhoon.org.cn

1 Introduction

The genesis and development of tropical cyclones (TCs) occur mainly over the open ocean. Owing to the lack of conventional observations in these remote areas, detecting the location of a TC center depends mostly on the use of satellite data (Dvorak, 1975, 1984, and 1993; Chen and Xiao, 1988 and 2005; Olander et al., 2004 and 2007; Velden et al., 2006; Wimmers and Velden., 2010). Because of the temporal irregularity in the spacing of images and the comparatively low resolution of passive microwave imagery, stationary satellite cloud images are generally used in operational TC analysis (Wimmers and Velden, 2010). Previous studies have developed experiential methods for locating TC centers using stationary satellite data (Dvorak, 1975, 1984, and 1993; William et al., 1987; Velden et al., 1989; Lee and Lin, 2001; Olander et al., 2004 and 2007; Zhang et al., 2005; Wei et al., 2009; Wimmers and Velden, 2010). Among these, Dvorak technique is the most popular technology worldwide with regards to estimating TC intensity in an operational setting (Dvorak, 1975, 1984, and 1993). The center location rule in Dvorak technique is to depict TC development as several special TC cloud patterns, with the TC center empirically fixed for each pattern. In effect, TC center location is simplified to determine the pattern to which the current TC cloud shape belongs. Although this method is widely used operationally, it lacks objectivity and the degree of precision varies with the operator, which can cause uncertainty in operational applications. To overcome these shortcomings, it is necessary to improve the objectivity and automation of estimating the TC center location. Accordingly, recent studies have considered how to objectively and automatically identify cloud patterns using Dvorak technique.

Lee and Lin (2001) developed the Elastic Graph Dynamic Link Model to provide an automatic pattern-

matching solution in Dvorak technique. Based on the extension of dynamic link architecture as a neural framework and its integration with the active contour model, the contours of 64 extracted TC patterns were remembered. Therefore, locating the TC center is simplified into contour extraction and graph matching of TC contour patterns. Using this approach, 120 hurricanes over the Atlantic Ocean between 1990 and 1998 were located; the bias was within 3 km for those samples with a clear "eye." However, this method requires clear and accurate extracted TC pattern contours. Furthermore, there was a lack of experimental data with which to test the method in operation. Olander et al. (2004) implemented an objective and automatic TC center location approach called the Advanced Objective Dvorak Technique (AODT). This method utilizes time-interpolated short-term track forecasts as a first guess for the location of the storm center. Then, a Laplacian analysis scheme is employed to search for sharp, spatially concentrated gradients in the infrared (IR) brightness temperature fields to identify possible eye locations. Subsequently, Olander and Velden (2007) utilized an objective storm center determination scheme and cloud pattern determination logic to remove the subjectivity from the intensity estimation process, based on matching TC patterns. TC centers were fixed based on the properties of different scene types. This development removed issues associated with subjective judgment; however, the location scheme contained complex mathematics and image processing algorithms. In 2011, the Automated Rotational Center Hurricane Eye Retrieval (ARCHER) algorithm was proposed by Wimmers and Velden (2010). The algorithm is able to find the center of rotation using spirally oriented brightness temperature gradients in TC banding patterns in combination with gradients along the ring-shaped edge of a possible eye. For TCs with estimated low to moderate vertical wind shear, the accuracy (root mean square error, RMSE) of ARCHER-estimated center positions is 17 km (9 km for category 1–5 hurricanes). In cases with estimated high vertical shear, the accuracy of ARCHER-estimated center positions is 31 km (21 km for category 2–5 hurricanes). The algorithm is also suitable for use with IR cloud images.

The spiral cloud belt is an important feature in TC cloud imagery (Liu et al., 1997; Xie et al., 1997; Liu et al., 2001; Zhang et al., 2005; Han and Wu, 2007). Accordingly, many studies have extracted the skeleton of the TC spiral cloud and fitted a logarithmic spiral line to locate the TC center (Liu et al., 1997; Xie et al., 1997; Liu et al., 2001; Zhang et al., 2005; Wang, 2006; Jin, 2008). The logarithmic spiral is a self-similar spiral curve for which the radius grows exponentially with the polar angle, and the relation between radius and angle is logarithmic (Willoughby, 1978; Wong et al., 2004, 2007, 2008, and 2009; Yurchak, 2007). Liu et al. (2003) proposed that TCs should be located in the area near the highest gradient of TC cloud-top brightness temperature. In tests using seven no-eye samples, the mean absolute error of this mathematical morphology method was about 50 km. Wang et al. (2002) suggested that a TC can be assumed to be a rigid object, because of its high speed of movement and rotation. Accordingly, based on the theory of rigid-body dynamics, the TC center could be located where the rotation vector is zero. However, the speed of a TC's rotation is not high and its movement is complex, meaning it is difficult to regard a TC as a rigid body. Thus, using this approach, the precision in locating the center is questionable.

In the present work, we propose a technique called spiral cloud belt matching (SCBeM). Using this approach, a dynamic TC Cloud Belt Template (CBT) is constructed based on an analysis of the extracted TC Cloud System (TCCS), after the fusion of multi-channel satellite images. The CBT, with specific width, length, rotation direction and shape, is used to match the real TC cloud belt to locate its center. This may provide an additional solution for automatically and objectively locating the TC center.

The rest of this paper is organized as follow. The data are presented in Section 2. The fusion of multi-band satellite images and TCCS extraction in a research setting are presented in Section 3. Section 4 describes the CBT construction and matching location technique in detail. Validation and evaluation of the method are presented in Section 5; finally, a summary of the key conclusions and discussion are provided in Section 6.

2 Data

FY-2C was the first operational stationary meteorological satellite mission launched by China. It carries a scanning radiometer that has five channels, including infrared bands 1–3 (IR1–IR3) (10.3–11.3, 11.5–12.5, and 3.5–4.0 μm, respectively), a water vapor band (6.3–7.6 μm), and a visible band (0.55–0.90 μm). This study analyzes the digital IR1 and visible and water vapor imagery obtained by FY-2C between 2012 and 2016. The data were supplied by the National Satellite Meteorological Center of the China Meteorological Administration (CMA). The area covered is approximately 55°N–10°S, 100°–160°E. The spatial and temporal resolutions of the imagery are approximately 4.5 km and 0.5 h, respectively. In addition, the CMA and Joint Typhoon Warning Center (JTWC) best track are used to validate the present work, as well as ARCHER and Advanced Dvorak Technique (ADT). TC center longitude and latitude, as well as TC intensity (in terms of maximum sustained winds, MSW), are included in the best track and real-time data sets. The observation times were 0000, 0600, 1200, and 1800 UTC. Only those images corresponding to the best track locations were used.

CMA TC category definitions are used here (Yu et al., 2013), which includes tropical depression (TD) (10.8 $\leqslant$MSW$\leqslant$17.1 m/s), tropical storm (TS) (17.2$\leqslant$MSW $\leqslant$24.4 m/s), severe tropical storm (STS) (24.5$\leqslant$MSW

⩽32.6 m/s), typhoon (TY) (32.7⩽MSW⩽41.4 m/s), severe typhoon (STY) (41.5⩽MSW⩽50.9 m/s), and super typhoon (SuperTY) (MSW⩾51 m/s). Generally, the spiral cloud belt is well formed when a TC is stronger than TD level. Therefore, in the following analysis, only TCs that were stronger than a TD were analyzed.

3 Fusion of multi-band cloud images and extraction of the TCCS

To save computing resources, the analysis region on a limited-size domain was segmented from the raw image, as follows. First, the first-guess position was obtained using the most recent forecast position or the TC real-time location extrapolated from the National Meteorological Center (NMC) of China. Second, taking the first-guess position as the center, a square area with a side length of 10° was segmented from the raw image. The length of each side of the square was an empirical value that ensured the current TC center was inside the fixed domain. Proceeding with this fixed area, we carried out the following operations.

3.1 Fusion of multi-band cloud images

TCCSs have better organization and clearer features than the surrounding environment. Image performance varies for the different bands owing to their different wavelengths (Fig. 1). The TCCS boundary was clear in IR1 and the visible channel (Fig. 1(a), (c)), but was obscure in the water vapor channel (Fig. 1(b)). The land boundary was clear in the visible channel (Fig. 1(c)) and obscure in the IR1 and water vapor channels (Fig. 1(a), (b)). To highlight the TCCS for extraction, the three band images (Fig. 2(a)–(c)) were fused (Fig. 2(d)) after binary processing. A fixed threshold value was adopted in the binary processing procedure. Here the threshold value is set as the 25th percentile of the pixel value for the whole image (Wang, 2006). If the pixel value is greater than or equal to the threshold value, it is set to 1; otherwise, it is set to 0. Figure 2(a)–(c) shows the binary processing results for the images in Fig. 1(a)–(c).

The purpose of image fusion is to enhance the TCCS boundary without missing or changing any features of the TC spiral skeleton. There was obvious brightness temperature variance between the TCCS and its surroundings. To clearly identify the boundary of the TCCS, the Local Variance Fusion (LVF) algorithm was used to analyze the adjacent pixel correlation (Qiang et al., 2003; Tao et al., 2006). Local characteristics can reflect the most important information differences when fusing multi-band images. LVF computes each pixel variance in a specified size of window traversed over the entire image pixel by pixel. On the variance map, each central pixel value of the image is replaced by the pixel value with the higher variance. Equations (1–2) are used to fuse the IR1, water vapor, and visible bands in order. The final fusion result is shown in Fig. 2d. Equation (1) is used to calculate the local variance in a specific window centered at the pixel point to be fused, and Eq. (2) is the final fusion value at the same pixel point,

$$\sigma_A = \frac{1}{J \times K} \sum\nolimits_{m \in [-(J-1)/2,(J-1)/2, n \in [-(K-1)/2,(K-1)/2]]} \left[A(x+m,y+n) - \overline{A(x,y)}\right]^2, \quad (1)$$

$$FV = \begin{cases} A(x,y), \text{ if } \sigma_A > \sigma_B \\ B(x,y), \text{ otherwise} \end{cases}, \quad (2)$$

where A and B are the images to be fused, σ_A is the local variance in a specific window of image A, and σ_B is the corresponding variable in B, both centered on point (x,y). $A(x,y)$ and $B(x,y)$are the pixel values. $\overline{A(x,y)}$ is the mean value in the local area at $A(x,y)$. J and K represent the size of the fusion window (in this study, both J and K are equal to 3), and m and n represent the pixel movement in the fusion window. FV is the final fusion value at (x,y).

Figure 2(d) shows the fusion result of the images in Fig. 2(a)–(c). It has a clearer TCCS boundary than that for any single band performance, with most cloud clutter around the TCCS being removed. This makes it possible to easily distinguish the TCCS from the whole analysis area.

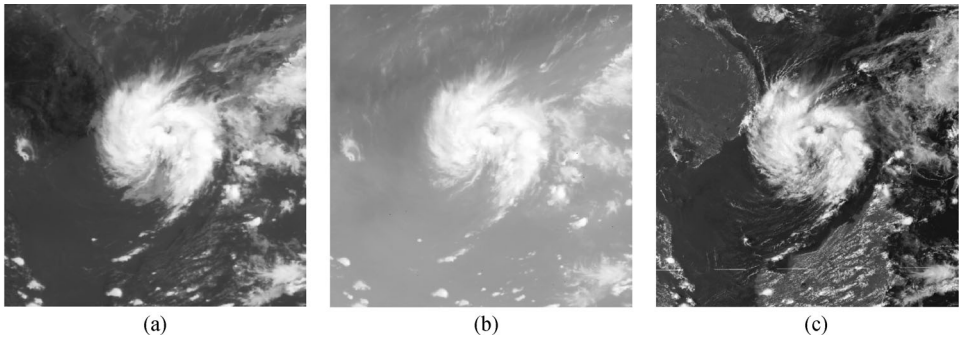

(a) (b) (c)

Fig. 1 TC cloud images in different satellite bands: (a) IR1, (b) water vapor, and (c) visible band images, at 0600 UTC on 29 March 2012.

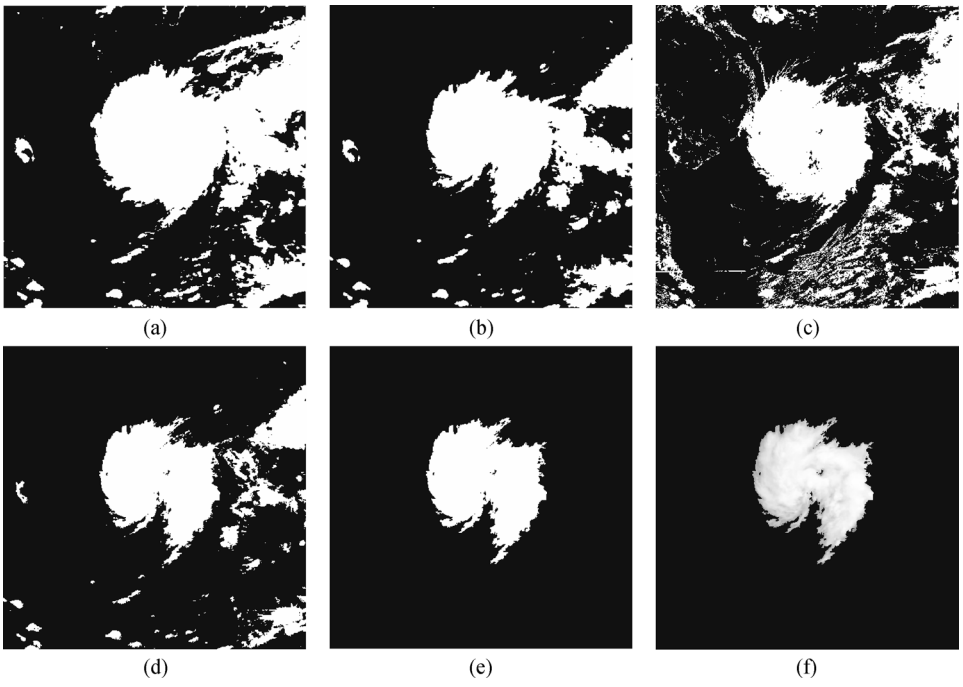

Fig. 2 TCCS extraction procedure. Binary processed images are shown for the (a) IR1 band, (b) water vapor band, and (c) visible band. Panel (d) is the fusion of the three bands, (e) is the separated binary TCCS, and (f) is the final separated TCCS from the IR1 image. All images are for the same time as indicated in Fig. 1.

3.2 TCCS extraction

TCCSs are much larger than cloud systems in the surrounding environment. Therefore, in the analysis area the maximum block extracted from the fused result (Fig. 2(e)) could be identified as the TCCS. To eliminate the incorrect inclusion of small and connected scattered and sporadic cloud in the complex environment, which may affect the identification of the TCCS, simple erosion and dilation were carried out to remove other unrelated cloud clusters. According to the binary image of the extracted TCCS, the same part was separated from the IR1 image (Fig. 2(f)), which was used in the subsequently applied location technique.

Overall, the TCCS was extracted from the IR1 image and the possible impact of the surrounding clutter was removed. This positive result enabled the identification of the TC center and is important in ensuring the precision of the automated center-fixing method.

4 CBT definition and matching localization

4.1 CBT definition and construction

The shape of a TC spiral cloud belt is assumed to follow a logarithmic spiral line (Dvorak, 1975, 1984, and 1993; Chen and Ding, 1979; Chen and Xiao, 1988 and 2005; Olander et al., 2004; Olander and Velden, 2007). This assumption is widely used operationally, such as in Dvorak technique. Willoughby (1978), Wong et al. (2004, 2007, 2008, and 2009) and Yurchak (2007) defined TC cloud belts or cloud-rain belts as logarithmic spirals. The polar equation is given by

$$r = ae^{b\theta}, \tag{3}$$

where a and b are TC-specific constants (Wong et al., 2004, 2007, 2008, and 2009). The parameter b describes the angle between the tangent and the radius from the center to any point on the logarithmic spiral. The parameter a characterizes the tightness of the logarithmic spiral line.

The polar equation can be translated to a rectangular coordinates system:

$$\begin{cases} x = ae^{b\theta}\cos\theta \\ y = ae^{b\theta}\sin\theta \end{cases}. \tag{4}$$

Expanding the logarithmic spiral line to the logarithmic spiral belt centered at (c_x,c_y) for its normal form, the expressions can be written as follows:

$$\begin{cases} x = (a-\omega_0)e^{b(\theta+\theta_0)}\cos(\theta+\theta_0) + \mathrm{c}_x \\ y = (a-\omega_0)e^{b(\theta+\theta_0)}\sin(\theta+\theta_0) + c_y \end{cases}, \tag{5}$$

where x and y are the coordinates of each point at the boundary of the spiral cloud belt centered at (c_x,c_y). ω_0

varies from 0 to ω, representing the outer and inner lines of the logarithmic spiral belt, respectively; i.e., the value of ω controls the width of the TC spiral cloud belt. b controls the shape of the logarithmic spiral belt. The length of the cloud belt is controlled by the parameter θ, with θ_0 being the initial phase angle. That is, the initial orientation and size of the TC spiral cloud belt is determined by the parameters c_x,c_y, θ_0, θ, a, b, and ω_0; these affect the template field of coverage and the final location result directly.

4.1.1 Determination of b

The parameter b should be determined to control the shape of the CBT. The shape of the TC spiral cloud belt is assumed to follow the 10° logarithmic spiral (Dvorak, 1975, 1984, and 1993). Therefore, the value of b is set as the tangent of 10° (0.1763). The TC spiral cloud belt shape is affected by its intensity. Generally, development of a TC involves tightening of the spiral and widening of the spiral space; hence, b increases with the stage of development of the TC. In the present work, the logarithmic spiral angle is assumed to vary between approximately 9° and 11°, so b varies between 0.16 and 0.19. Finally, b is set as 0.16, 0.17, 0.17, 0.18, and 0.19 to represent the shape of the spiral CBT for TCs of different intensities, covering the range from TS to SuperTY (Table 1).

Table 1 Values of b for the TC spiral cloud belt template for different intensity categories

TC category	b
TS	0.16
STS	0.17
TY	0.17
STY	0.18
SuperTY	0.19

4.1.2 Determination of a and ω_0

The parameters a and ω_0, which control the width and size of the CBT, need to be determined. The size and width of the cloud belt of a particular TC vary over time. Therefore, the parameters a and ω_0 should be set to specific values according to the real-time TCCS size. It is known that TC size correlates with TC intensity (Merrill, 1984; Lu et al., 2011). Merrill (1984) found that this correlation is weak, and Lu et al. (2011) reported that the correlation is positive. Song and Klotzbach (2016) and Wu et al. (2015) pointed out that the correlation is complicated and nonlinear. However, all TCs demonstrate that the size of a TC tends to increase as its intensity strengthens over its lifespan. Hence, a wider and larger CBT should be used for larger and stronger TCs, whereas a narrower and smaller CBT should be used for smaller TCs. However, there are also outliers. For example, although TC Bilis in 2006 was very large, with a mean size of 257 km and a maximum size of 331 km, its maximum intensity was only 26 m/s, whereas TC Saomai (2006) had a maximum intensity of 72 m/s but a mean size of only 170 km (Lu et al., 2011). In the construction of our CBT, width and size are determined by both TC intensity and TCCS size. The TC size index calculated from TCCS may assign a strong TC to a relatively small size class in its intensity group. Small STYs and medium TSs can have the same size. Therefore, such outliers could also be suitable classified.

In this study, TC size is reported in terms of the number of pixels of the extracted TCCS. As this number is large and difficult to measure, a standard TC area index (STCAI) is put forward to replace it, calculated using Eqs. (6–7). This index represents a relative TC size in different intensity groups over a long time. In Eq. (6) the standard deviation of TCCS size is computed among all samples and in Eq. (7) the STCAI is computed according to the standard deviation, real time current TCCS size, and the mean TCCS size value of all samples. The STCAI distribution between 2012 and 2015 is shown in Fig. 3,

$$\sigma = \sqrt{\frac{1}{N}\sum_{i=1}^{N}(x_i-\mu)^2}, \tag{6}$$

$$\mathrm{STCAI} = (C_\mathrm{s}-\mu)/\sigma, \tag{7}$$

where N is the sample number, x_i is the TCCS size for each sample, μ is the mean size of all samples, σ is the standard deviation of TCCS size, and C_s is the current real-time TCCS size.

Figure 3 shows differences in the STCAI distribution between the different TC intensity groups. The median values are 0.17, 0.19, 0.32, 0.19, and 0.13 for the TS to SuperTY intensity categories, respectively. For all samples together, the median is 0.20. To some degree, this result shows that the size of a TCCS increases as it develops. However, once the TC reaches TY level, as it continues to develop the spiral cloud belt rolls more tightly and the TCCS size decreases slightly. This conclusion is in accordance with the statistical relation between TC size and intensity outlined by Lu et al. (2011), in which TC size was measured as the mean radius of 34 kt surface winds using JTWC best track data (Lu et al., 2011). Therefore, based on the median and the lower quartile of the STCAI distribution, the TCs in each intensity category are further classified into three groups: small (S), median (M), and large (L) (Table 2).

Knowing the TC size (diameters of ~550 and <1000 km) and spiral direction (inward anticlockwise in the Northern Hemisphere) (Wong et al., 2004; Lu et al., 2011), a is set to between 20 and 40, varying between different TC intensity and size groups. Assuming other parameters are constant, ω varies between 5 and 25. The results show that when $\omega<15$, the template is too narrow and it cannot express the TCCS correctly, while when $\omega>20$ the

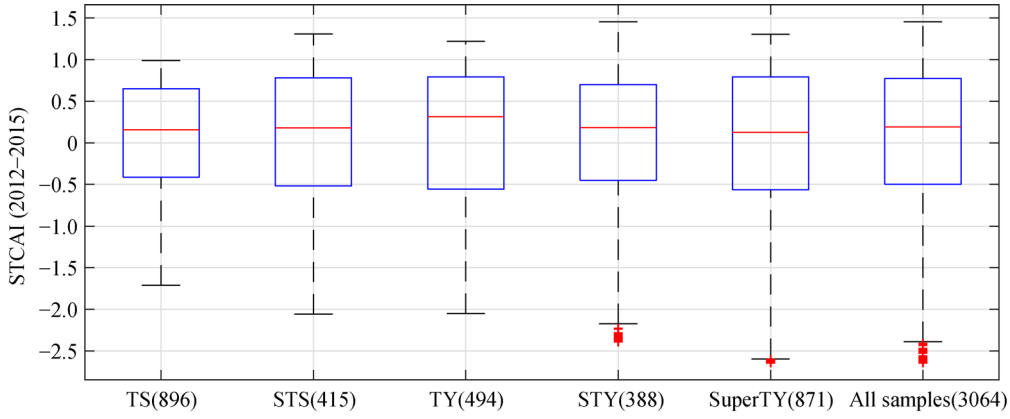

Fig. 3 Boxplots showing the STCAI distribution for different TC intensity groups for 2012–2015. The red horizontal line represents the median, and the upper and lower limits of the blue boxes represent the 75th and 25th percentiles, respectively. The short red lines represent the outliers.

template is too wide and overlaps with itself, or has a diameter over 1000 km. Finally, the parameters a and ω_0 are fixed for the three different classes in each category (Table 2).

4.1.3 Determination of θ and θ_0

It is necessary to evaluate θ and θ_0, which control the CBT length and the beginning phase angle, respectively. In Dvorak technique, which employs either visible or IR images, the length of the TC spiral cloud belt is an important factor (Dvorak, 1975, 1984, and 1993). This indicates a close correlation between TC intensity and spiral cloud belt length, which enables an approximate determination of the parameter θ for each intensity group (Table 3) (Dvorak, 1975, 1984, and 1993).

In general, a TC is spread out at the tail according to its cyclonic features and spiral performance (Chen and Ding, 1979); therefore, for most TCs the largest part of the TCCS is in the quadrant in which the tail lies. According to the TCCS distribution in eight sectors, it is possible to determine the phase angle where the tail is found, θ_t. Thus, the beginning phase angle θ_0 can be set as $\theta_t - \theta$, where θ is the TC spiral cloud belt length. Finally, the CBT is constructed using the parameters a, b, ω_0, θ_0, and θ.

4.2 Space querying, matching, and locating the TC center

Based on the above template, the space querying and matching are carried out in a fixed square area with side length of 100 km, centered on the first-guess position. A side length of 100 km was chosen because the first guess

Table 2 Values of a and ω_0 for the different size and intensity groups

TC category	STCAI range	Size	a	ω_0
TS	STCAI ⩽ −0. 5	S	20	[0 15]
	−0.5 < STCAI ⩽ 0.2	M	25	[0 16]
	STCAI > 0.2	L	30	[0 17]
STS	STCAI ⩽ −0. 5	S	25	[0 16]
	−0.5 < STCAI ⩽ 0.2	M	30	[0 17]
	STCAI > 0.2	L	35	[0 18]
TY	STCAI ⩽ −0. 55	S	30	[0 17]
	−0.55 < STCAI ⩽ 0.4	M	35	[0 18]
	STCAI > 0.4	L	40	[0 19]
STY	STCAI ⩽ −0.45	S	25	[0 16]
	−0.45 < STCAI ⩽ 0.2	M	30	[0 18]
	STCAI > 0.2	L	35	[0 20]
SuperTY	STCAI ⩽ −0.5	S	25	[0 17]
	−0.5 < STCAI ⩽ 0.25	M	30	[0 18]
	STCAI > 0.25	L	35	[0 19]

Table 3 Value of θ for the different TC intensity groups

TC category	θ
TS	2.5π
STS	2.5π
TY	2.75π
STY	2.75π
SuperTY	3.0π

position is derived from the most recent forecast or 6 h extrapolation, which is generally less than 100 km from the 'real' center. This domain is then traversed pixel by pixel to set up multiple CBTs that are subsequently evaluated to determine the best one.

To evaluate the degree of matching between the real TC spiral cloud belt and the constructed template, an evaluation function was created. In terms of the performance of colder and uniform mean gray values in the region of the TC spiral cloud belt, but warmer and uneven gray values in the TC center and the outer region of its spiral cloud belt, the mean brightness temperature in the cloud belt is the major factor characterizing the real TC. Equation (8) defines the evaluation function for the template matching assessment. The value of F represents the best signal to assess the degree to which the current template matches the real one; the smaller the value, the better the template matches the real TC cloud belt,

$$F = \frac{\sum T_{BB}(ij)}{num}, \tag{8}$$

where *num* is the number of pixels in the current CBT, T_{BB} (i, j) is the temperature of the current pixel, and i and j represent the row and column numbers in the CBT.

4.3 SCBeM in an operational setting

SCBeM can be applied in an operational setting. Its system framework is shown in Fig. 4.

The framework requires real-time satellite information regarding TC intensity (real-time or 6 h ago) and location (6 and 12 h ago). Such information is routinely made available by most operational TC forecast centers. First, the first-guess position is obtained by extrapolating the locations 6 and 12 h ago, or by using a 6-h forecast. Second, taking the first-guess position as the center, the image analysis area is segmented from the raw image. Then, through fusion of the IR1, water vapor, and visible bands, the TCCS is extracted. Note that the visible band is not used at night. Third, using the TC intensity (real-time or 6 h ago) together with the infrared satellite information analysis of extracted TCCS, a CBT is constructed. Finally, the evaluation function value is computed pixel by pixel in the fixed area, and the pixel center with the smallest evaluation function value (F) is fixed as the TC center.

5 Analysis and evaluation of SCBeM

5.1 Accuracy of location with SCBeM

Using SCBeM, we carried out an experiment using data for 126 TCs that occurred between 2012 and 2016 (1957 samples). The tracks and spatial distributions of the sample TCs are shown in Fig. 5. In constructing the CBT, we used the STCAI distribution of TCs that occurred during 2012–2015. Accordingly, the locations of the 97 TCs in 2012–

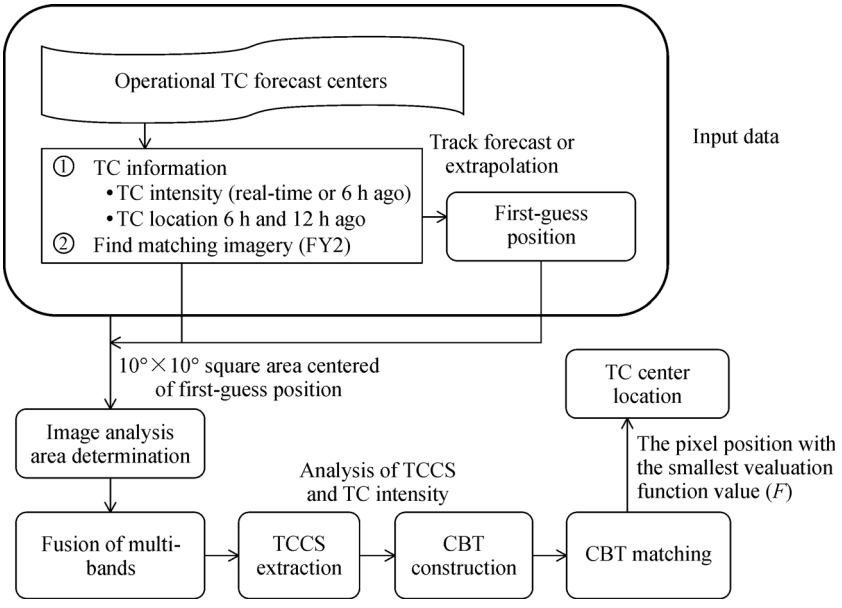

Fig. 4 SCBeM system framework. The framework includes information acquisition, TCCS extraction, CBT construction, and CBT matching.

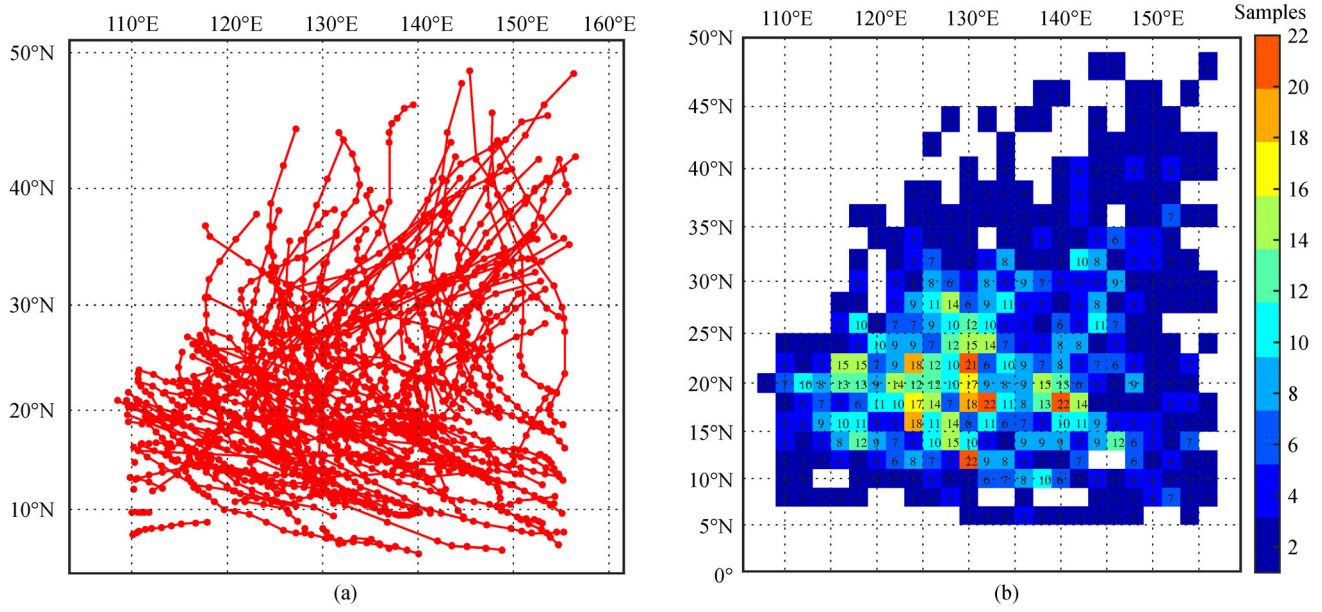

Fig. 5 TC tracks (a) and the spatial distribution (b) of samples used in SCBeM location for TCs over the period 2012–2016. The grid size is 2° × 2° and the numbers in the grid squares in the right-hand figure indicate the sample size.

2015 can be regarded as a dependent test, and the locations of another 29 TCs in 2016 can be regarded as an independent test. Relative to the CMA best track, for the dependent test the ME is 50 km, the mean absolute error (MAE) of SCBeM is 54 km, the RMSE is 64 km, and the total percent of automated center-fixes within 0.5° latitude (P0.5) is 58% (Table 4). For the independent test, the ME is 55 km, the MAE is 57 km, the RMSE is 66 km, and P0.5 is 54%. The location error of the independent test is slightly higher than that of the dependent test. In terms of performance for different intensity categories, when the TC intensity was at or above the TY level, the accuracy of the location was better than that for weaker systems.

To assess the impact of search box size on location accuracy, two sets of experiments using search boxes of sides 50 and 200 km in length were conducted using the 2016 events. The location ME was 55 and 79 km, respectively (321 samples from 29 TCs), which suggests that location accuracy is not better for a smaller search box. The size and shape of the constructed CBT play the key roles in the final determination of the TC center.

Figure 6 shows some 'good' (Figs. 6(a)–(d)) and 'bad' (Figs. 6(e)–(f)) individual cases using the new technique. Figure 6(a) shows TC Dujuan (1521), which was located east of the Philippines and moving to the north-west at 0600 UTC on 25 September 2015; its intensity was 45 m/s, its eye was clear, and its TCCs was in a standard 10° logarithmic spiral form, with a location error of 4.2 km. As shown in Fig. 6(b), TC Halola (1512) was moving north-west at 1200 UTC on 20 July 2015. Although its intensity was just 20 m/s and at TS level, its TCCS was small and round, showing a clear logarithmic spiral. There was very good template matching and the location error was 8.7 km. Figure 6(c) shows TC Nepartak (1601) at 1800 UTC on 6 July 2016 and Fig. 6(d) shows TC Meranti (1614) at 1200 UTC on 12 September 2016. At these times, they were both located to the south-east of Taiwan and moving north-west. Their eyes were clear with intensity above SuperTY, and location error was less than 20 km. Figure 6(e) shows TC Nida (1604) at 1200 UTC on 30 July 2016. At that time, Nida had existed for one day, the intensity was 20 m/s, and its TCCS was

Table 4 Errors in SCBeM location estimates for 2012–2015 TCs (compared with CMA best track). ME indicates the median error and MAE indicates the mean absolute error

TC category	ME/km	MAE/km	RMSE/km	P0.5	*N*
TS	50	57	67	57	526
STS	55	61	71	51	300
TY	55	58	65	51	334
STY	48	50	57	61	262
SuperTY	34	41	48	76	214
All	50	54	64	58	1636

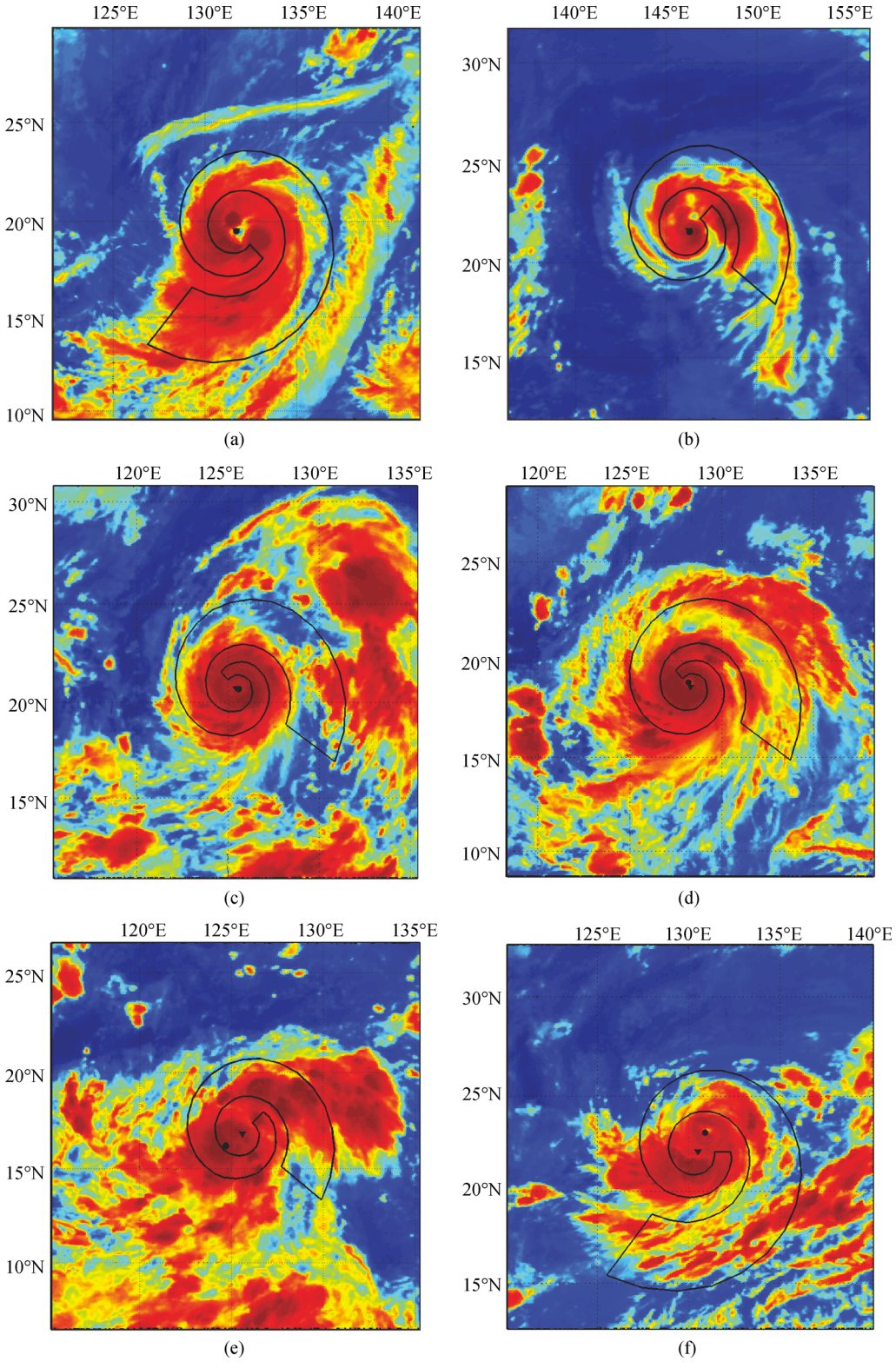

Fig. 6 TC center location for 'good' (a–d) and 'bad' (e and f) samples. The black logarithmic spirals in the figures are constructed CBTs. The black filled circle is the best track position, and the black inverted triangle is the location determined by the SCBeM. (a) TC Dujuan (1521) at 0600 UTC on 25 September 2015, (b) TC Halola (1512) at 1200 UTC on 20 July 2015, (c) TC Nepartak (1601) at 1800 UTC on 6 July 2016, (d) TC Meranti (1614) at 1200 UTC on 12 September 2016, (e) TC Nida (1604) at 1200 UTC on 30 July 2016, and (f) TC Lionrock (1610) at 0000 UTC on 26 August 2016.

somewhat messy. The location accuracy in this case was low, at 120 km. Figure 6(f)shows TC Lionrock (1610) at 0000 UTC on 26 August 2016, when it was also moving north-west. Although its eye was clear, its TCCS had been strongly disturbed by the vertical wind shear in the north-west sector and the TCCS was deformed. The location error was 119 km. The vertical wind shear in all of the above cases was low (< 10 m/s) except that in Fig. 6(f).

Analysis of the location accuracy of SCBeM in different latitudinal regions and different vertical wind shear groups demonstrates that the accuracy at low latitudes ($< 25°$ N) and low vertical wind shear (< 10 m/s) is better than that for other samples. The median error is 45–47 km, which is smaller than that of other samples. In ARCHER-2 (Wimmers and Velden 2016) the median center-fix error is 49 km when only the infrared windows are used. South of 25°N corresponds to the tropics, where a TC always has tight, clear, standard logarithmic spiral banding when it attains TS level with low to moderate vertical wind shear, which is suitable for application of the SCBeM method. For TCs with a deformed TCCS, whether affected by vertical wind shear, terrain, westerly flow, or some other factor, matching becomes difficult and location accuracy is poor. In some cases, the error can be as large as 200 km, meaning SCBeM is not suitable.

The spatial difference between the location results and the best track for TC Peipah (1404) in 2014 is shown in Fig. 7. The mean location error was about 35 km, the maximum was 62.6 km, and the minimum was 4.8 km. While tracking north-west, the spiral cloud belt of Peipah kept a standard logarithmic spiral form and turned inward anticlockwise. The standard form of the spiral cloud belt means it can be located well automatically.

5.2 Comparison of SCBeM with other objective techniques

Considering the clear differences between the CMA and JTWC best track data sets (Yu et al., 2006; Ren et al., 2011) and consistent with the above evaluations part, the location accuracies of SCBeM, ARCHER, and ADT are compared based on CMA best track data for events in 2014–2016 (Table 5). ARCHER performs better in ME and SCBeM is better in MAE. Microwave (85–92 GHz) images, ASCAT, and geostationary satellite imagery (visible, IR, and SWIR) are all used in the ARCHER technique (Wimmers and Velden, 2016). Using IR imagery alone, the ME of ARCHER is 49 km (Wimmers and Velden, 2016), which is close to that of SCBeM. Therefore, the accuracy of SCBeM could be acceptable in an operational setting; however, its precision still needs to be improved, for example by integrating more observations.

The SCBeM technique considers only the general form (log spiral morphology) of a TC cloud system and the brightness temperature distribution. Based on the current TC size and intensity obtained from infrared (IR) imagery and a TC operational warning agency, a dynamic TC CBT is constructed to query and match the real TCCS. The best match point determination depends on the evaluation

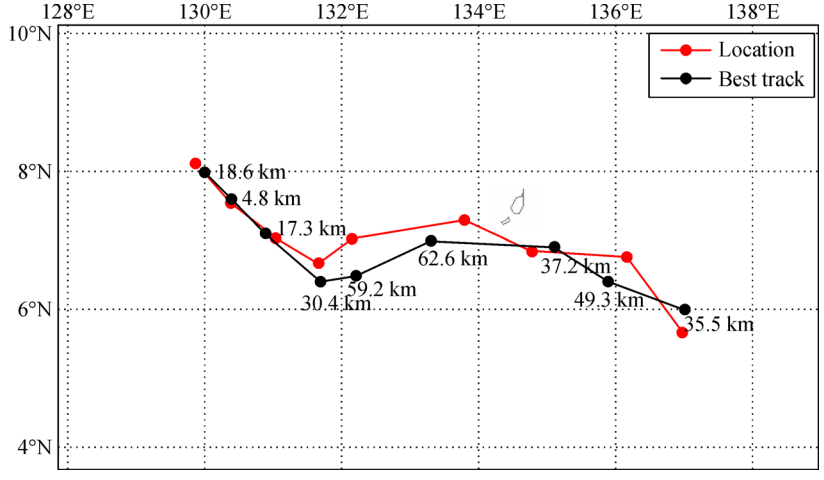

Fig. 7 Comparison between the location results and the best track for TC Peipah (1404) in 2014. The number next to each best track point indicates the location error in kilometers.

Table 5 Location error, when compared with CMA best track, for SCBeM, ARCHER, and ADT using events over the period 2014–2016. *N* denotes the sample size. ME and MAE definitions are those given in Table 4

Method	ME/km	MAE/km	*N*
SCBeM	52	55	1157
ARCHER	32	65	781
ADT	40	74	1419

function value calculated from the brightness temperature distribution along the CBT. In contrast, ARCHER finds the center of rotation using spirally oriented brightness temperature gradients in the TC banding patterns, in combination with gradients along the ring-shaped edge of a possible eye (Wimmers and Velden, 2010 and 2016). This method is the same for ADT, as a version of ARCHER is used in ADT. Accordingly, both eye patterns and any banded circulation patterns are accounted for. In addition, the passive microwave imagery used in ARCHER, which can reveal convective organization and eyewall structure that would otherwise be obscured by cloud tops, plays a crucial role in the location of central dense overcast cloud type in a TC (Wimmers and Velden, 2010 and 2016). When a TC has no well-defined organized banding pattern, SCBeM cannot be applied successfully. ARCHER has a similar problem, as vertical shear can adversely affect the organization of the TC and disrupt the conventional spiral-eye configuration that ensures the algorithm can be successfully applied (Wimmers and Velden, 2010). Therefore, although the location accuracy of SCBeM is not better than that of ARCHER, SCBeM could be used as an additional solution for automatically and objectively locating the TC center. SCBeM is a simple approach that requires no complicated mathematical calculations and is a better choice for those TC operational agencies in the case that microwave images, ASCAT, or other observations are not available in a timely manner. It can also automatically show the viewer an intuitive and optimal spiral fit associated with a center fix estimate.

6 Conclusions and discussion

This paper proposes a TC center location technique for TCs, named SCBeM. Through the fusion of multi-band geo-satellite images, the TCCS is extracted from the whole image area. Based on the TCCS, a CBT is constructed to approach the real TC. The CBT is expressed well using a set of parameters (Tables 1–3) that characterize its shape, width and size, length, and initial phase. An experiment involving the location of 126 TCs from the years 2012 to 2016 was conducted. Compared with the CMA best track, the ME and MAE of SCBeM are 50 and 54 km, respectively, for dependent samples from 2012 to 2015. For independent samples from 2016, the ME and MAE of SCBeM are 54 and 57 km, respectively. These values are close to those for ARCHER using IR imagery compared with NHC best track. This objective and automated technique has the potential to be used operationally; furthermore, the algorithm is simple and the accuracy is promising.

SCBeM is built on the hypothesis that the form of TCCS follows the 10° logarithmic spiral. In reality, differences in TC intensity, latitudinal area, and the environmental field all lead to variability in the shape of TC spiral cloud belts. For weaker TCs, or those that experience severe shear or that make landfall, the cloud belt is commonly messy, without any obvious convergence, and the TC cloud structure may not retain its spiral shape. SCBeM may not be suitable in such situations. When TCs are near the coastline or making landfall, their locations should be obtained from surface observations, such as ground-based radar. For TCs showing severe vertical wind shear, location information should be obtained from microwave satellite data, such as in ARCHER. Furthermore, after the CBT is constructed in SCBeM, the space querying and template matching are carried out in a fixed square area of side length 100 km, centered at the first-guess position. Hence, the precision of the first-guess position plays an important role in the precision of SCBeM. In cases where a TC enters the westerlies, is fast-moving, or is transforming to an extratropical cyclone, the first-guess position can be far from the real TC center, resulting in poor accuracy for SCBeM. Furthermore, TC intensity 6-h ago is used when real-time TC intensity is unavailable. However, the TC intensity category may change during this 6-h period, and so cause errors in CBT construction and affect the final location. In the current SCBeM, there is no pre-analysis of the reliability of the location accuracy. However, following ARCHER (Wimmers and Velden, 2010), in the future SCBeM should also include a ‘default’ option (a predefined first-guess position) to fall back onto when the detection signal is determined to be too weak. The detection signal could be defined as the evaluated value for the current estimated center. The vertical wind shear value, terrain, and westerly flow will be considered in the evaluation, and more accurate parameters will be explored in construction of the CBT.

Acknowledgements The CMA and JTWC best track archives were obtained from Typhoon Online website and NDBC website respectively. The real-time archives of ARCHER and ADT were downloaded from SSEC. WISC website. This study was supported by the Key Projects of the National Key R&D Program (No. 2018YFC1506300), the National Basic Research Program of China (No. 2015CB452806), and the Key Program for International S&T Cooperation Projects of China (No. 2017YFE0107700), the Natural Science Foundation of Shanghai (No. 15ZR1449900), and the National Natural Science Foundation of China (Nos. 41675116, 41575046, 41775065, and 41405060).

References

Chen L S, Ding Y H (1979). General Features and Structure of Tropical Cyclones—An Introduction to the Western Pacific Typhoon. Beijing: Science press, 1–45 (in Chinese)

Chen W M (2005). Application of Satellite Imagery in Tropical Weather Analysis and Prediction. Satellite meteorology (The second edition). Beijing: Meteorological press, 401–415 (in Chinese)

Chen W M, Xiao W A (1988). Atlas of satellite cloud image Analysis, Atmospheric Physics department Technical Report. Nanjing Meteorology Institute, 11–17 (in Chinese)

Dvorak V (1975). Tropical cyclone intensity analysis and forecasting from satellite imagery. Mon Weather Rev, 103(5): 420–430

Dvorak V (1984). Tropical cyclone intensity analysis using satellite data. NOAA Technical Report, NESDIS 11, 47

Dvorak V, Smigielski F (1993). Tropical Cyclone Center Location on Satellite Imagery, A Workbook on Tropical Clouds and Cloud Systems Observed in Satellite Imagery 1993, National Environmental Satellite, Data, and Information Service training materials. Translated by Guo W, Lu N M, Sun D L, and Shi C X, 1996, Beijing: Meteorological Press, 217–240 (in Chinese)

Han Y, Wu R S (2007). On the spiral structure of typhoon. Journal of Nanjing University: (Nat Sci Ed), 6(43): 572–580 (in Chinese)

Jin M (2008). Extraction and representation of cyclone image feature and typhoon center location. Dissertation for the Master's Degree. Kunming: Tianjin, Tianjin University, (in Chinese)

Lee R T, Lin J K (2001). An elastic contour matching model for tropical cyclone pattern recognition. IEEE Trans Syst Man Cybern B Cybern, 31(3): 413–417

Liu K, Huang F, Luo J (2001). The study on automatic tracking method of typhoon spiral cloud bands. Computer Engineering, 27(10): 152–154 (in Chinese)

Liu Z G, Lin K Y, Guo A M, Cheng Y (1997). The extraction of satellite cloud image feature. Research and Development of Computer, 9: 689–693 (in Chinese)

Liu Z G, Zou L, Wu B (2003). The center location of eyed typhoon in satellite cloud image. Pattern Recognition and Artificial Intelligence, 16(3): 334–337 (in Chinese)

Lu X Q, Yu H, Lei X T (2011). Statistics for size and radial wind profile of tropical cyclones in the western North Pacific. Acta Meteorol Sin, 25(1): 104–112

Merrill R T (1984). A comparison of large and small tropical cyclones. Mon Weather Rev, 112(7): 1408–1418

Olander T L, Velden C S, Kossin J P (2004). The Advanced Objective Dvorak Technique (AODT)-continuing the journey In: 26th AMS Conf. on Hurricane and Tropical Meteorology, Miami, FL, USA

Olander T L, Velden C S (2007). The advanced Dvorak technique: continued development of an objective scheme to estimate tropical cyclone intensity using geostationary infrared satellite imagery. Wea. Forceasting, 22(2): 287–298

Qiang Z X, Peng J X, Wang H Q (2003). Remote sensing image fusion based on local deviation of wavelet transform. J Huazhong U Sci Tec, 31(6): 89–91

Ren F M, Liang J, Wu G, Dong W, Yang X (2011). Reliability analysis of climate change of tropical cyclone activity over the western north Pacific. J Clim, 24(22): 5887–5898

Song J J, Klotzbach P J (2016). Wind structure discrepancies between two best track datasets for western north Pacific tropical cyclones. Mon Weather Rev, 144(12): 4533–4551

Tao B J, Wang J R, Xu J P (2006). Study on image fusion based on different fusion rules of wavelet transform. Infrared technology, 28 (7): 431–434

Velden C, Harper B, Wells F, Beven J L II, Zehr R, Olander T, Mayfield M, Guard C, Lander M, Edson R, Avila L, Burton A, Turk M, Kikuchi A, Christian A, Caroff P, Mccrone P (2006). The Dvorak tropical cyclone intensity estimation technique: a satellite-based method that has endured for over 30 years. Bull Am Meteorol Soc, 85: 353–385

Velden C S, Olson W S, Roth B (1989). Tropical cyclone center-fixing using DMSP SSM/I data. In: 4th Conf. Sat. Meteor., San Diego, CA, Amer. Meteor. Soc.: 36–39

Wang F N (2006). The researches of segmentation and central location of typhoon cloud department based on satellite cloud image. Dissertation for the Master's Degree. Kunming: Yunnan Normal University, 1–120 (In Chinese)

Wang Y Y, Ye Z, Sun Y C (2002). Typhoon center locating using rotation feature matching method. Journal of Image and Graphics, 7A (5): 491–494 (in Chinese)

Wei K, Li Y X, Jing Z L, Liang X D, Lu X Q (2009). Typhoon cloud pattern discovery based on SOM clustering. Infrared, 30(12): 16–24 (in Chinese)

William T C, Elsberry R L, Chan C L (1987). An objective technique for estimating present tropical cyclone locations. Mon Weather Rev, 115 (6): 1073–1082

Wimmers A J, Velden C S (2010). Objectively determining the rotational center of tropical cyclones in passive microwave satellite imagery. J Appl Meteorol Climatol, 49(9): 2013–2034

Willoughby H E (1978). A possible mechanism for the formation of hurricane rain bands. J Atmos Sci, 35(5): 838–848

Wimmers A J, Velden C S (2016). Advancements in objective multi satellite tropical cyclone center fixing. J Appl Meteorol Climatol, 55 (1): 197–212

Wong K Y, Yip C L, Li P W, Wan T W (2004). Automatic template matching method for tropical cyclone eye fix. In: Proc. 17th Int. Conf. Pattern Recognition (ICPR'04), Cambridge, United Kingdom, 650–653

Wong K Y, Yip C L, Li P W (2007). A novel algorithm for automatic tropical cyclone eye fix using Doppler radar data. Meteorol Appl, 14 (1): 49–59

Wong K Y, Yip C L, Li P W (2008). Automatic tropical cyclone eye fix using genetic algorithm. Expert Syst Appl, 34(1): 643–656

Wong K Y, Yip C L (2009). Identifying centers of circulating and spiral vector field patterns and its applications. Pattern Recognit, 42(7): 1371–1387

Wu L G, Tian W, Liu Q Y, Cao J, Knaff J A (2015). Implications of the observed relationship between tropical cyclone size and intensity over the western North Pacific. J Clim, 28(24): 9501–9506

Xie J Y, Ai Z Y, Gao Y (1997). Automatic recognition algorithm of spiral curve in position typhoon center. J Softw, 8(6): 398–403 (in Chinese)

Yu H, Chen P Y, Li Q Q, Tang B (2013). Current capability of operational numerical models in predicting tropical cyclone intensity in the western north Pacific. Wea Forceasting, 28(2): 353–367

Yu H, Hu C M, Jiang L Y (2006). Comparison of three tropical cyclone strength datasets. Acta Meteorol Sin, 64(3): 357–363 (in Chinese)

Yurchak B S (2007). Description of cloud-rain bands in a tropical cyclone by a hyperbolic-logarithmic spiral. Russ Meteorol Hydrol, 32(1): 8–18

Zhang Q P, Lai L L, Sun W C (2005). Location of tropical cyclone center with intelligent image processing technique. ICMLC 2005. Lect Notes Artif Intell, 3930: 898–907